第 35 卷第 5 期
2019 年 5 月

无 机 化 学 学 报
CHINESE JOURNAL OF INORGANIC CHEMISTRY

Vol.35 No.5
769-779

有双重固硫作用的 PEDOT 包覆 MnO_2 纳米管阴极用于高性能的锂硫电池

葛 优 潘沛锋 彭 霞 刘瑞卿* 朱红丽 冯晓苗* 沈清明 黄镇东 马延文
(南京邮电大学有机电子与信息显示重点实验室暨先进材料研究所(IAM),南京 210023)

摘要：制备了 α-MnO_2 纳米管作为硫的宿主材料,将硫填充到 α-MnO_2 管的中空部分,并通过原位聚合法在 α-MnO_2 外层包覆一层薄层聚(3,4-乙烯二氧噻吩)(PEDOT)进一步束缚硫。这样一种双重固硫的阴极材料 S@α-MnO_2-PEDOT 在锂硫电池中体现出了高的性能。在电流密度 1 675 mA·g^{-1}(1C)下循环 200 圈,容量为 774.4 mAh·g^{-1},且在电流密度为 3 350 mA·g^{-1}(2C)下容量达 854.1 mAh·g^{-1},体现出良好的循环稳定性和倍率性能。这些显著的性能得益于阴极材料新颖的结构。在这种结构中,α-MnO_2 纳米管不仅能对硫起到物理限制作用,而且增强了硫宿主材料和多硫化物间的化学相互作用。同时,PEDOT 的引入增强了含硫纳米复合材料的导电性,并进一步减少了由于体积变化和多硫化锂的过度溶解引起的硫的损失。

关键词：锂硫电池；MnO_2 纳米管；PEDOT；水热自组装
中图分类号：TB34 **文献标识码**：A **文章编号**：1001-4861(2019)05-0769-11
DOI：10.11862/CJIC.2019.063

Dual-Confined Sulfur Cathodes Encapsulated in MnO_2 Nanotubes and Wrapped with PEDOT for High-Performance Lithium-Sulfur Batteries

GE You PAN Pei-Feng PENG Xia LIU Rui-Qing* ZHU Hong-Li
FENG Xiao-Miao* SHEN Qing-Ming HUANG Zhen-Dong MA Yan-Wen
(*Key Laboratory for Organic Electronics and Information Displays & Institute of Advanced Materials (IAM), Nanjing University of Posts & Telecommunications, Nanjing* 210023, *China*)

Abstract: α-MnO_2 nanotubes were developed as host material to fill with sulfur in their tubular hollow space, and then the sulfur were further encapsulated by a thin layer of poly (3,4-ethylenedioxythiophene) (PEDOT) exterior coating via an *in situ* polymerization process. Such a dual-confined sulfur cathode, denoted as S@α-MnO_2-PEDOT, showed high performance in lithium-sulfur batteries. It could reach a capacity of 774.4 mAh·g^{-1} at a current density of 1 675 mA·g^{-1} (1C) after 200 cycles and 854.1 mAh·g^{-1} at a current density of 3 350 mA·g^{-1} (2C), manifesting excellent cycling stability and rate capability. The outstanding performances are attributed to the new architecture. In the novel architecture, α-MnO_2 nanotubes not only provide the physical confinement for sulfur, but also enhance the chemical interaction between the sulfur host material and polysulfides. Simultaneously, PEDOT was introduced to enhance conductivity of sulfur-containing nanocomposites and further reduce the loss of sulfur due to volumetric change and the excessive dissolution of lithium polysulfides.

Keywords: lithium-sulfur batteries; MnO_2 nanotube; PEDOT; hydrothermal self-assembly

收稿日期:2019-01-02。收修改稿日期:2019-02-19。
国家自然科学基金(No.51772157,61504062,21575069)、江苏省自然科学基金(No.BK20150863,BK20160890)、江苏省研究生创新工程项目(No.CXZZ12_0461)和南京邮电大学基金项目(No.NY217004)资助。
*通信联系人。E-mail:iamxmfeng@njupt.edu.cn,iamrqliu@njupt.edu.cn

0 Introduction

At present, among the rechargeable batteries, lithium-sulfur batteries are expected to satisfy various energy storage and conversion demands because of high theoretical specific capacity of sulfur element (1 675 $mAh \cdot g^{-1}$) and specific energy density of Li-S batteries (2 600 $Wh \cdot kg^{-1}$), abundant resources in natural, low cost, and environmentally friendly[1-7]. However, the practical application of lithium-sulphur batteries is still hindered by some drawbacks. For instance, (a) large volumetric change of sulfur cathode during charge and discharge process leading poor cycling performance[8]; (b) the excessive dissolution of polysulfides and subsequent "shuttle effect" resulting in specific capacity decline rapidly[9-15]; (c) insulative sulfur and lithium polysulfide with low electronic conductivity reducing the rate capacities of Li-S batteries[16-17].

In order to solve the above problems, a number of strategies have been developed to optimize the composition and the structure of the sulfur cathode. Most host materials for sulfur are carbonous materials, such as micro-/mesoporous carbon[18], carbon spheres[19], carbon nanotubes/nanofibers[20], and graphene[21]. These host materials not only improve the electronic conductivity of sulfur-based electrodes, but also capture the polysulfides to retard the shuttling of soluble polysulfides. On the other hand, conducting polymers, such as poly (3,4-ethylenedioxythiophene) (PEDOT)[22-23], polyaniline (PANI)[24] and poly (acrylic acid) (PAA)[25], have also been used as host materials for sulfur attributing to their high conductivity, flexibility and thermal stability. However, the intermolecular interactions between lithium polysulfides (LiPSs) and carbonous materials or conducting polymers are weak because of physically confining LiPSs due to their non-polar characteristic, the LiPSs diffuse out of the cathode and eventually migrate to the anode easily.

Recently, sulfur host materials exhibiting strong chemical interactions with LiPSs have been studied and appeared to be an effective approach to stabilizing the capacity, including modified carbonaceous materials[26], functional polymeric materials[27]. Introduction of electronegative N atoms into the carbon lattice, such as mesoporous N-doped carbon, induces asymmetric charge distribution. This affects the net polarity, creating sites for binding LiPSs[28-29]. Moreover, metal oxides such as MnO_2[30], TiO_2[31], TiO[32], V_2O_5[33] and Al_2O_3[34], and metal sulfides including TiS_2[35], WS_2[36] and CoS_2[37] have been proposed as effective lithium polysulfides trappers by utilizing the strong chemical adsorption. As a polar oxide, MnO_2 has high binding energy between MnO_2 and LiPSs because of the presence of stronger polar chemical bond. Extensive efforts have been devoted to the development of nanostructures for trapping LiPSs, such as MnO_2 nanowires[38], MnO_2 nanosheets[39] and MnO_2 nanoparticles[40]. However, these solid structures restrict the content of sulfur loading and cannot solve the large volumetric change of sulfur cathode. Meantime, conductivities of metal oxides are low, leading to low sulfur utilization and poor rate performance. Therefore, the combination of polar hollow materials and conducting matrix with rationally designed structures is a desired strategy to enhance the electrochemical properties of sulfur cathode. So far, the research of hollow MnO_2 nanotubes for sulfur host is comparatively rare. Only the PPy-MnO_2 coaxial nanotubes have been synthesized to solve the above problems due to the high conductivity of PPy, the strong chemical adsorption and hollow structure of MnO_2 nanotubes[41]. However, in the preparation procedure, the MnO_2 nanowires were used as template and the hollow MnO_2 nanotubes were prepared by acid etching. The complex preparation process significantly affected the manufacturability of the sulfur cathode. Therefore, there is still a challenge to design innovative method and nanostructures for efficaciously encapsulation of sulfur.

Herein, the hollow α-MnO_2-PEDOT nanotubes were prepared through a facile template-free hydrothermal self-assembly *in situ* polymerization to immobilize sulfur. In the composite structure, the MnO_2 hollow nanotubes not only enhance the sulfur

loading and accommodate volumetric change of sulfur, but also provide combined role of chemical and physical adsorption for lithium polysulfides. The chemical adsorption attribute to Mn-S bond which is conducive to limit lithium polysulfides. The physical adsorption is produced by hollow nanotube morphology. Besides, S@MnO_2 combining with PEDOT could enhance the conductive of S@α-MnO_2-PEDOT and reduce the excessive dissolution of polysulfides. After combining with the conductive polymer PEDOT, the S@MnO_2-PEDOT nanocomposites electrode revealed the excellent discharge specific capacity of 774.8 mAh·g^{-1} at 1.0C after 200 cycles, which effectively perfects the electrochemical properties of Li-S batteries.

1 Experimental

1.1 Synthesis of urchin-like α-MnO_2 nanotubes

All the reactants and solvents were analytical grade and used without further purification. Urchin-like α-MnO_2 nanotubes were produced by hydrothermal method. In a typical process, 0.17 g of $KMnO_4$ was dispersed in 18 mL of deionized water (DI) to form a clear solution under magnetic stirring for 30 min. Subsequently, 2 mL of HCl (2 mol·L^{-1}) was added to the clear solution dropwise under magnetic stirring. It was then transferred into an autoclave and heated to 120 ℃ for 12 h. The hydrothermal product was collected by centrifugation and rinsed several times with DI and ethanol.

1.2 Synthesis of S@α-MnO_2 composites

The mixtures of prepared urchin-like α-MnO_2 nanotubes and sulfur were sealed and heated to 155 ℃ for 10 hours. Then, the mixtures were heated to 250 ℃ under argon flow for 30 min in tube furnace to eliminate the sulfur on the outside surface of the α-MnO_2 nanotubes by evaporation. The resulting S@α-MnO_2 composites with the sulfur loading of 71.09%(*w*/*w*) were obtained, according to the thermogravimetric analysis (TGA).

1.3 Synthesis of S@α-MnO_2-PEDOT

A simple in situ polymerization process was used to coat the PEDOTs on the surface of S@α-MnO_2 composite. Typically, 50 mg S@α-MnO_2 composites were dispersed into the different quantity (4, 2, 1 mg) of 3,4-ethylenedioxythiophene (EDOT) solution at room temperature. Then different quantity (12.50, 6.25, 3.12 mg) of oxidant $FeCl_3$ solution was added dropwise sequencingly. After stirring for 6 hours, the final product was collected by centrifugation, washed by distilled water several times, and then dried at 60 ℃ overnight.

1.4 Characterization

XRD measurements were carried out on a Philip XRD X′PERT PRO X-ray diffractometer operating at 40 kV and 40 mA, and using Cu *Kα* radiation (λ= 0.154 18 nm). The diffraction patterns were performed in the 2*θ* range of 10° ~80° . The structure and morphology were characterized by SEM (Hitachi S-4800 at 10 kV) and TEM (Hitachi 7700 at 100 kV). High-resolution TEM (HRTEM) images were recorded on FEI Talos F200X field-emission transmission electron microscope operated at 200 kV. Raman spectroscopy was carried out using a Renishaw inVia Raman microscope with a 532 nm laser with exposure time of 10 s, the laser power was reduced to 1% to minimize the sublimation of sulfur due to the laser heating. Chemical bonding nature was analyzed by X-ray photoelectron spectroscopy (PHI 5000 Versa Probe). Thermogravimetric analysis was used to determine the sulfur content of the material on a TGA instrument (NETZSCH STA-449 C) employing a heating rate of 10 ℃·min^{-1} from room temperature to 700 ℃ under a nitrogen flow.

CR2032-type coin cells were assembled in a glovebox filled with argon. The working electrodes were prepared by mixing 70% (*w*/*w*) active materials, 20% (*w*/*w*) acetylene black and 10% (*w*/*w*) polyvinylidene fluoride (PVDF) binder in N-methyl pyrrolidinone (NMP). The slurries were homogeneously coated on to aluminum foil current collectors. The electrodes were dried at 60 ℃ for 12 h under vacuum. Subsequently, the electrodes were cut into disks with a diameter of 13 mm. A piece of lithium foil was used for the combined counter and reference electrodes. 1.0 mol·L^{-1} lithium bis(trifluoromethanesulfonyl)imide (LiTFSI) in 1,3-dioxolane and 1,2-dimethoxyethane

(volume ratio, 1∶1) with 1%(*w*/*w*) $LiNO_3$ as an additive was used as the electrolyte. The $LiNO_3$ was added to help passivate the surface of the lithium anode and reduce the "shuttle effect". Celgard 2400 was used as a separator film. The cycle performances, rate capability and galvanostatic charge/discharge tests were carried out on LAND CT2001A in a potential range of 1.5~2.8 V (vs Li/Li^+). The specific capacity was calculated based on the weight of sulfur. Cyclic voltammetry (scan rate: 0.2 $mV \cdot s^{-1}$, cut-off voltage: 1.5 ~2.8 V) and electrochemical impedance spectra (frequency range from 100 kHz to 10 mHz) were measured with an electrochemical workstation VMP3.

2 Results and discussion

2.1 Structure characterization

The formation mechanism of hollow urchin-like morphology of manganese dioxide can be explained by the process of Ostwald maturation. In general, permanganic acidradical is unstable on thermodynamics and it is easy to be reduced to manganese dioxide. Therefore, the reaction occurred rapidly in an acidic environment and at a high temperature under hydrothermal condition. At the beginning of the reaction, a large number of MnO_2 crystal nuclei condensed into MnO_2 microspheres and MnO_2 nanorods grew outwards along the surface of the microsphere, the formation of the hollow urchin-like structure was attributed to the gradual disappearance of the core. The formation of MnO_2 nanotubes was mainly due to the etching of MnO_2 nanorods by hydrochloric acid. In the hydrothermal condition, hollow urchin-like morphology of MnO_2 can be reflected in the intensification of the etching. The redox reaction can be described by Equation (**1**) as follows.

$$4MnO_4^- + 4H^+ = 4MnO_2 + 3O_2 + 2H_2O \quad (\mathbf{1})$$

The scanning electron microscopy (SEM) images of α-MnO_2 (Fig.1(a~c), Fig.S1, Supporting Information) exhibit the 3D structure of urchin-like morphology at different magnifications. The urchin-like microspheres assembled by a large number of short-sized nanotubes of manganese dioxide dispersed from the center to the outside can be observed from Fig.1(a,b). From Fig.1c, the manganese dioxide nanotubes with hollow structure can be seen clearly as green ellipses shown. TEM images (Fig.1(d~e)) also revealed that the obvious hollow structure of α-MnO_2 nanotubes and the nanotubes had a diameter of approximately 120 nm.

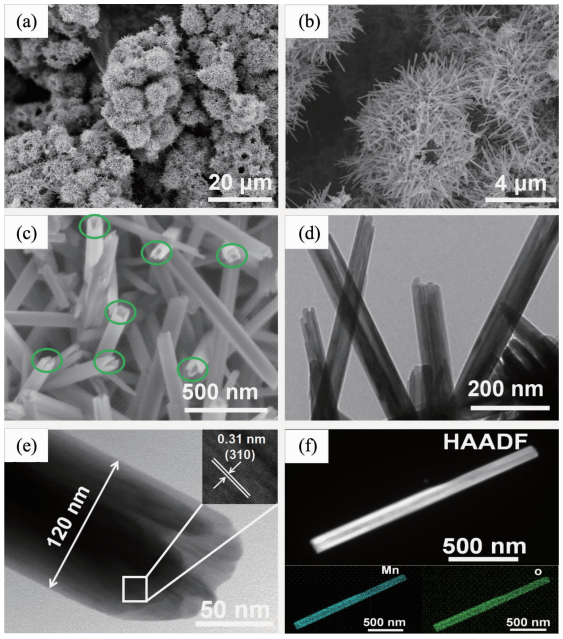

Fig.1 (a~c) SEM images of urchin-like α-MnO_2 under the different magnifications; (d, e) TEM images of the α-MnO_2 under different magnifications; (f) HAADF-STEM image and corresponding elemental mappings of α-MnO_2 nanotube

The lattice fringe with an interplanar spacing of about 0.31 nm that corresponded to the (310) plane of α-MnO_2 was further identified from the inset of Fig.1e. The high-angle annular dark field scanning transmission electron microscopy (HAADF-STEM) image and elemental mappings of MnO_2 nanotubes exhibit the element distribution of Mn and O along the length of nanotube in Fig.2f.

After the melt-diffusion stage, the S@α-MnO_2 nanotubes morphology (Fig.2a) was maintained well except for the rough surface compared with the pristine MnO_2 nanotubes (Fig.1c). To give further insight into the morphology and structure of the S@α-MnO_2, TEM analysis has been carried out. Fig.2b reveals that the solid rods, indicating the sulfur was successfully encapsulated in hollow tubes of MnO_2. After the solid rods of S@α-MnO_2 were coated by PEDOT, there was obviously cladding on the outer surface as shown in Fig.2c, and the enlarged image (Fig.S2) shows the wrapped nanotube of S@α-MnO_2-PEDOT with a diameter of approximately 140 nm. Fig.2d further reveals the presence of PEDOT and the thickness was approximately 10 nm under the mass ratio of S@α-MnO_2 composites and EDOT with 50∶2. For comparison, other different mass ratios (50∶1, 50∶4) were also carried out, their thicknesses were 5 and 20 nm, respectively (Fig.S3). Moreover, the HAADF-STEM and TEM elemental mappings confirmed the existence and homogeneous distribution of Mn, O, S and C elements in S@α-MnO_2 (Fig.2e) and S@α-MnO_2-PEDOT (Fig.2f), respectively. The high voltage and volatilization of some sulfur during TEM testing resulted in the hollow structure to some extent.

The X-ray diffraction (XRD) pattern indicates tetragonal crystal system of hollow urchin-like α-MnO_2. The α-MnO_2 had tunnel structures which was one of five known mineral polymorphs of manganese oxide. The crystal structure of α-MnO_2 was tunnel structures of [1×1] and [2×2] which being composed by single or double chain according to [MnO_6] octahedral along public edges[42]. As shown in the Fig. 3a, the main diffraction peaks of α-MnO_2 at around 12.9°, 17.9°, 28.6°, 37.5°, 42.0°, 49.8°, 56.3°, 60.1°, 65.4°, 69.4° and 73.2°, which was consistent with the diffraction peaks of the tetragonal crystal system of α-MnO_2 (PDF No.44-0141) reported in the literature[43]. The product had good crystallization because all diffraction peaks were sharp in Fig.3a. Also, the XRD patterns of S@α-MnO_2 and S@α-MnO_2-PEDOT were almost the same to that of elemental sulfur with

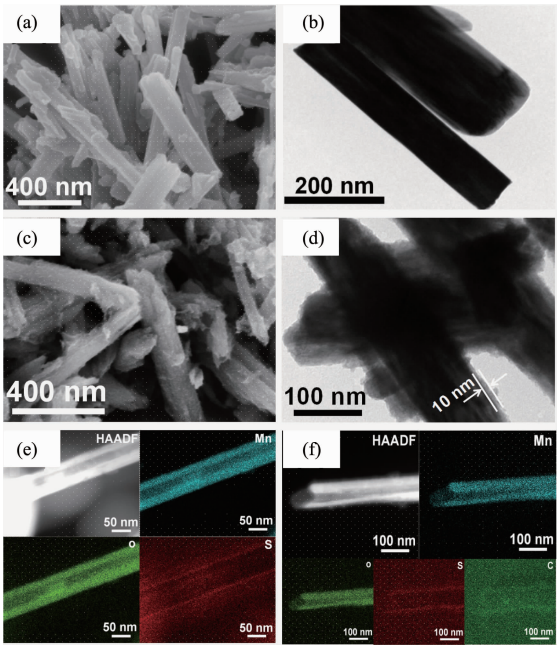

Fig.2　(a) SEM and (b) TEM images of S@α-MnO_2; (c) SEM and (d) TEM images of S@α-MnO_2-PEDOT; HAADF-STEM image and corresponding elemental mappings of (e) S@α-MnO_2 and (f) S@α-MnO_2-PEDOT

preponderant peaks at 23.02°, 26.26°, 27.65°, and 28.61°, indicating sublimed sulfur was successfully infiltrated into α-MnO_2 nanotubes and α-MnO_2-PEDOT composites, and the diffraction peaks were in good agreement with the standard cards of sulfur (PDF No. 08-0247) and manganese dioxide. Because of the existence of PEDOT, the diffraction peak intensity was weak compared with pure MnO_2. The sulfur contents of S@α-MnO_2-PEDOT composites with different mass ratio of S@α-MnO_2 composites and EDOT were demonstrated by thermogravimetric analysis (TGA) in Fig.S4. In the TGA, the sulfur volatilized when temperature reached ~160 ℃ showing steep weight loss and the slight weight loss around 500 ℃ could be attributed to the pyrolysis of PEDOT. In the control sample, the residual moisture content was about 3% (*w*/*w*). The TGA reveals that the sulfur contents (mass percentage) of S@α-MnO_2-PEDOT nanocomposites are 69.75% (50:1), 70.40% (50:2) and 71.91% (50:4). The Raman spectrum of S@α-MnO_2-PEDOT composites was as provided to investigate the structural information (Fig. 3b). The intensive peak at 1 443 cm^{-1} was chiefly due to the C-C stretching vibration of the thiophene ring, rooting in the neutral parts existing between the localized elementary excitations such as positive polarons or bipolarons generated upon doping[44-46]. The peaks consisted in 1 502 and 1 565 cm^{-1} were put down to the C=C asymmetric stretching vibrations of the thiophene rings in the middle and at the end of the chains, respectively[47]. The peak at 635 cm^{-1} was attributed to MnO_2. Moreover, There were obvious Raman spectra of pure sulfur at 152.9, 218.4 and 471.6 cm^{-1}, which corresponded to the vibration of S-S bond in S@α-MnO_2-PEDOT composites[48]. To prove the interaction of polysulfides with α-MnO_2 nanotubes, the XPS analysis of pristine α-MnO_2, the polysulfide and α-MnO_2 nanotubes were carried out. The XPS spectra of the whole spectrum of S@α-MnO_2-PEDOT and Li_2S_6@α-MnO_2-PEDOT are shown in Fig.S5. In Fig.3c, the Mn2$p_{3/2}$ spectrum showed two deconvoluted peaks at 641 and 642.3 eV, corresponding to Mn^{3+} and Mn^{4+} of pristine α-MnO_2, respectively[49]. As evident from Fig.3d, the oxidation of Li_2S_6 resulted in the partial reduction of Mn^{4+} to Mn^{3+} and Mn^{2+}. The peak intensity of Mn^{3+} significantly enhanced, and the new peak located at 640~641 eV, which could be assigned to the Mn^{2+} oxidation states. The results can be clearly seen further confirming the strong interaction of

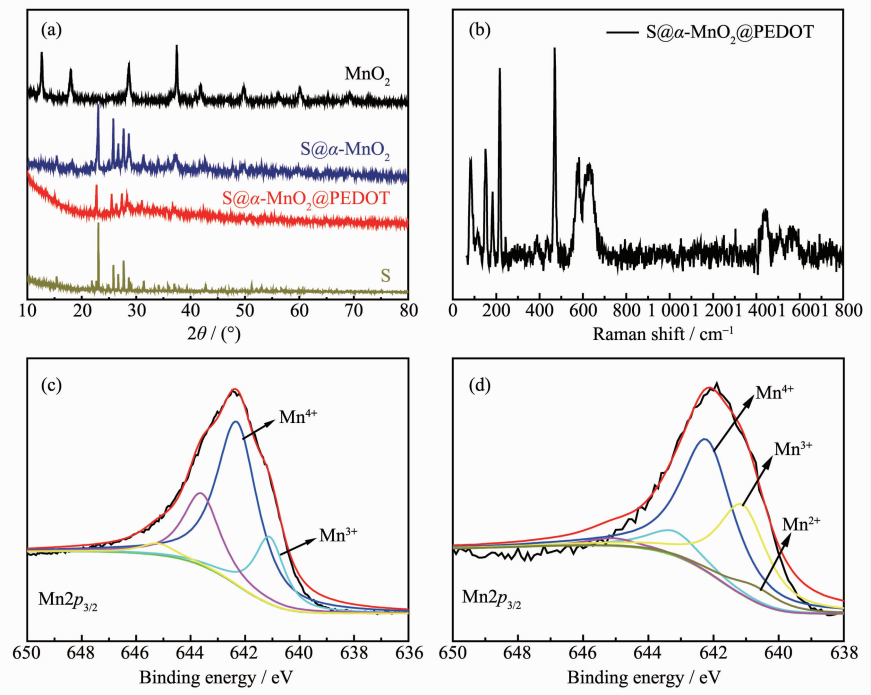

Fig.3 (a) X-ray diffraction patterns of pristine sulfur, α-MnO_2, S@α-MnO_2 and S@α-MnO_2-PEDOT; (b) Raman spectra of S@α-MnO_2-PEDOT; XPS spectra of (c) S@α-MnO_2-PEDOT and (d) Li_2S_6@α-MnO_2-PEDOT for Mn2$p_{3/2}$

polysulfides with MnO_2 nanotubes, which can load more sulfur species around the Mn ion and trap more soluble polysulfides[50].

2.2 Electrochemical performance

The electrochemical performances of the S@α-MnO_2 and S@α-MnO_2-PEDOT composites were illustrated in the following research. The first four cycles of the CV curves of S@α-MnO_2 and S@α-MnO_2-PEDOT nanocomposites are presented in Fig.4(a,b) in the potential range of 1.5 ~2.8 V at a scan rate of 0.2 $mV \cdot s^{-1}$. Unlike the CV curves of S@α-MnO_2, the CV curves of S@α-MnO_2-PEDOT had higher current, suggesting the better conductivity of S@α-MnO_2-PEDOT by introduction of PEDOT. However, both of CV curves showed representative reduction and oxidation characteristic peaks for the lithium-sulfur batteries, and the peaks were at almost the same positions. Two typical reduction peaks at around 2.0 and 2.24 V could be attributed to the multistep reduction reaction of sublimed sulfur[51]. The former was attributed to the reduction of S_8 to S_8^{2-}, and the latter was related to further transformation of soluble long-chain polysulfide (Li_2S_n, n =4 ~6) to produce insoluble short-chain polysulfides (Li_2S or Li_2S_2)[52]. In the oxidation process, the main peak at around 2.45 V corresponded to the reverse reactions of polysulfides back to S_8. There was a significant reduction peak of CV in the first circle between 1.5 and 1.8 V in Fig. 4b, which may be attributed to the formation of SEI film. Obviously, as the cycle proceeds, the cathodic

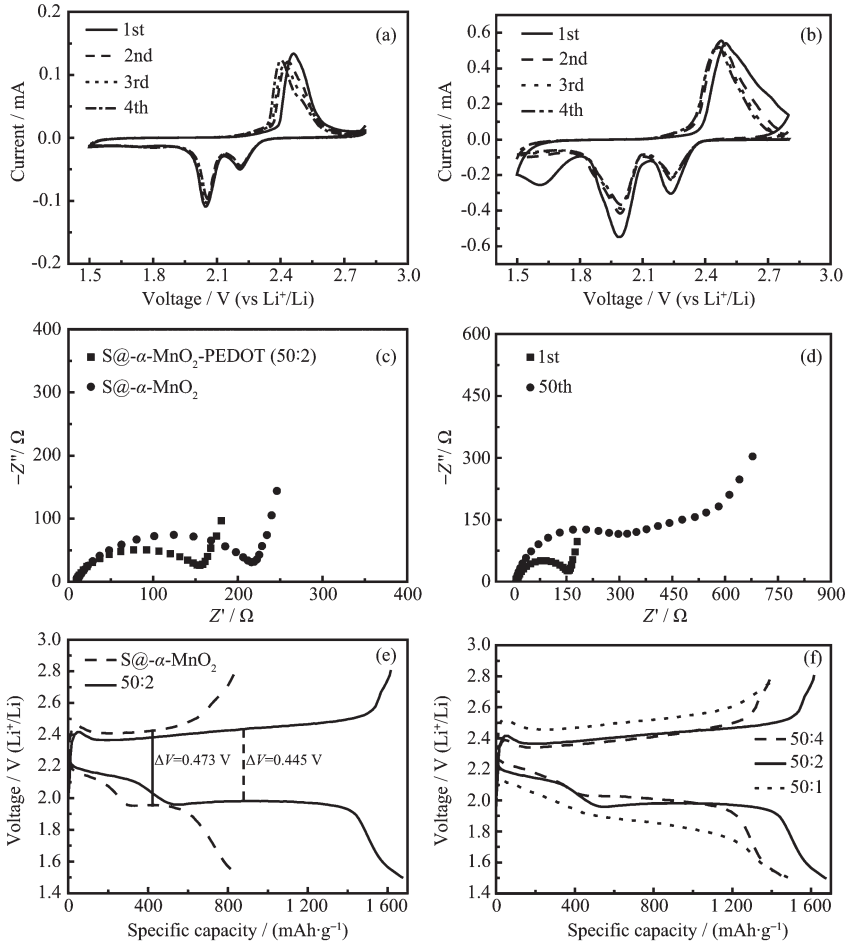

Fig.4　CV curves of (a) S@α-MnO_2 electrode and (b) S@α-MnO_2-PEDOT electrode for the first four cycles at a scan rate of 0.2 $mV \cdot s^{-1}$; (c) Nyquist plots of S@α-MnO_2 electrode and S@α-MnO_2-PEDOT electrode before cycling; (d) Nyquist plots of S@α-MnO_2-PEDOT electrode after cycling; (e) Initial discharge/charge voltage profiles of S@α-MnO_2 and S@α-MnO_2-PEDOT electrodes (50:2) at 1.0C; (f) Initial discharge/charge voltage profiles of S@α-MnO_2-PEDOT electrodes with different PEDOT contents at 1.0C

peaks were shifted to higher potentials and the anodic peaks were shifted to lower potentials, indicating an improvement of reversibility of S@α-MnO_2. To further investigate the dynamics of S@α-MnO_2 and S@α-MnO_2-PEDOT nanocomposite. As shown in the Fig.4c, the electrochemical impedance spectroscopy (EIS) measurement was emerged. It can be seen that the EIS spectra included a depressed semicircle in the high frequency region and a sloping line (Warburg impedance) in the low frequency region. The semicircle is attributed to the charge-transfer process, which corresponds to the resistance over Li^+ diffusion through the contacting interface between the electrolyte and active material electrode. The sloping line reflects a semi-infinite Warburg diffusion process[53]. The semicircle in the high frequency region is due to the interfacial charge transfer resistance (R_{ct}). It is obviously shown that S@α-MnO_2-PEDOT exhibited a lower R_{ct} (*ca.* 160 Ω) than that of S@α-MnO_2 (*ca.* 220 Ω), revealing that the S@α-MnO_2-PEDOT composites electrode has excellent electrical conductivity during the charge and discharge process and the presence of PEDOT in favor of electrochemical reaction kinetics. Fig.4d shows the EIS spectra of S@α-MnO_2-PEDOT electrode after cycling. After the 50th cycle, the resistance of S@α-MnO_2-PEDOT electrode was more than 300 Ω, which was larger than that after the 1st cycle, indicating a lower electronic conductivity because of the generation of LiPSs during cycling process.

Fig.4e shows initial discharge/charge voltage profiles of S@α-MnO_2 and S@α-MnO_2-PEDOT electrodes (50:2). It is observed that there were two plateaus at typical discharge process. The lower voltage plateau at *ca.* 2.0 V reflected the further reduction of high-order polysulfides to low-order polysulfides (Li_2S_n, $n<4$) and finally to insoluble lithium sulfides (Li_2S_2/Li_2S). In addition, the upper voltage plateau conformed with the conversion from S_8 to long chain polysulfides (Li_2S_8, Li_2S_6, or Li_2S_4). However, the charge plateau is related to the transformation from Li_2S_2/Li_2S to Li_2S_8/S_8, which agreed well with the CV analysis. The S@α-MnO_2-PEDOT composites electrode (50:2) showed the higher initial specific discharge capacity (1 672.2 mAh·g^{-1}) than that of S@α-MnO_2 electrode (868.1 mAh·g^{-1}). Importantly, the smaller voltage platform difference (0.445 V) of S@α-MnO_2-PEDOT electrode compared with the voltage platform difference (0.473 V) of S@α-MnO_2 electrode suggests that the electrochemical reaction reversibility of the S@α-MnO_2-PEDOT is higher relative to S@α-MnO_2 because of the presence of PEDOT. Fig.4f shows initial discharge/charge voltage profiles of S@α-MnO_2-PEDOT electrodes with different PEDOT contents. These S@α-MnO_2-PEDOT composites electrodes with different PEDOT contents show the initial specific discharge capacity values of 1 487.7 (50:1), 1 672.2 (50:2) and 1 465.7 mAh·g^{-1} (50:4).

As shown in Fig.5a, the rate capabilities of S@α-MnO_2-PEDOT composite electrodes with different PEDOT contents under different current densities. It was tested by varying current densities from 335 (0.2C) to 3 350 mA·g^{-1} (2.0C). The rate capabilities of S@α-MnO_2-PEDOT composites electrodes are much higher than that of S@α-MnO_2 electrode. It was clearly visible that the composite with mass ratio of 50:2 obtained the best rate performance. The discharge capacities were 1 582.8, 1 209.4, 1 000.1 and 854.1 mAh·g^{-1} at the current densities of 0.2C, 0.5C, 1.0C and 2.0C, respectively. When the current density was reduced back to 0.2C, the capacity was recovered to 1 108.6 mAh·g^{-1}, indicating that relatively good stability at different current densities. The cycling performance and coulombic efficiency of S@α-MnO_2 electrode at the different current densities (0.5C, 1C, 2C; 1C=1 675 mA·g^{-1}) are shown in Fig.5b. The initial discharge capacities were 1 248.7 (0.5C), 868.1 (1.0C) and 529.2 (2.0C) mAh·g^{-1}, respectively. And after 150 cycles, the capacities decayed to 549.2, 496.8 and 332.9 mAh·g^{-1} at 0.5C, 1.0C and 2.0C, respectively. The capacity retentions respectively are 44.0%, 57.2% and 62.9% . The coulombic efficiencies were basically above 97%. Apparently, it was important that α-MnO_2 nanotubes structure could effectively physically restrain the produced polysulfides and also had valid chemical bond of Mn-S to adsorb polysulfides efficiently, which promoting the utilization of the

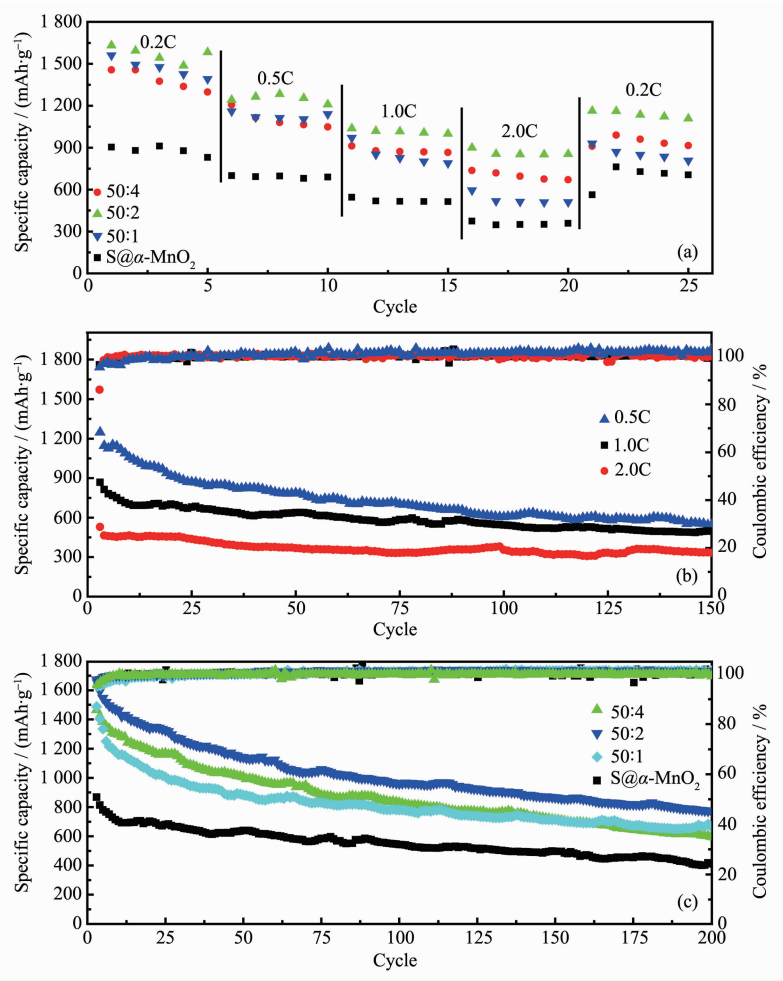

Fig.5　(a) Rate capabilities of S@α-MnO_2-PEDOT electrodes with different PEDOT contents; (b) Cycling performances of S@α-MnO_2 electrode at different current densities; (c) Cycling performances of S@α-MnO_2-PEDOT electrodes with different PEDOT contents at the current density of 1.0C

active material and the reaction kinetics. Fig.5c presents the cycle performances and coulombic efficiencies of S@α-MnO_2-PEDOT composite electrodes with different contents of PEDOT at the current densities of 1.0C. Among them, the initial specific discharge capacity values were 1 465.7 (50:4), 1 672.2 (50:2), 1 487.7 (50:1) and 868.1 (50:0) mAh·g^{-1}, respectively. Obviously, the S@α-MnO_2-PEDOT composite (50:2) has the most remarkable cycle performance. After testing 200 cycles, the specific capacity could still achieve 774.4 mAh·g^{-1}, and the coulombic effciency curve was relatively stable. The excellent electrochemical properties of S@α-MnO_2-PEDOT composites were attributed to dual function of MnO_2 nanotubes and conductive PEDOT buffer layer. In the hybrid composites, MnO_2 nanotubes and PEDOT layer not only could physically restrict the sulfur/polysulfides inside the inner hollow structure to prevent polysulfides from dissolving into the electrolyte and succedent shuttle effect, but also relieve the volume expansion of S during discharge/charge process and provided a convenient transport channel for ions[54]. Moreover, the bonding interaction between polysulfides and MnO_2 inhibited the chronic seeping of polysulfides and maintained the relative integrity of the electrode. In addition, highly conducting PEDOT layer provided efficient pathways for electron transport. The thicker PEDOT coating, the stronger the conductivity of the composite and more effective at binding sulfur, which resulted in the better electrochemical performance. However, the cycle performances of the S@α-MnO_2-PEDOT composite (50:4) and (50:1) were similar after

100 cycles. This may be ascribed to the fact that the thicker PEDOT coating has a slight effect on the migration of ions. Therefore, the most superior electrochemical properties of S@α-MnO_2-PEDOT composite (50:2) were presented. The presence of conductive PEDOT buffer layer, effective MnO_2 nanotubes matrix, bonding interaction between polysulfides and MnO_2, and synergistic effect among them yield a robust architecture for enhancing the electrochemical performances of lithium sulfur batteries.

3 Conclusions

In summary, a sulfur cathode has been prepared using hollow α-MnO_2 nanotubes and exterior PEDOT coating as host materials to immobilize sulfur and capture polysulfides. The hollow α-MnO_2 nanotube structure not only can accommodate volumetric change of sulfur, but also can provide convenient ion channels and physical constraint for sulfur/polysulfides. It also can effectively adsorb the polysulfides produced during charge-discharge process by the formation of chemical bond of Mn-S. Moreover, a buffer layer of PEDOT was covered on the surface of MnO_2 to further enhance the conductivity of the composite cathodes, accelerate electronic transmission, and boost stability of the composites. The S@α-MnO_2-PEDOT composites exhibited excellent electrochemical performance. It could reach a capacity of 774.4 $mAh \cdot g^{-1}$ at a current density of 1 675 $mA \cdot g^{-1}$ (1C) after 200 cycles and 854.1 $mAh \cdot g^{-1}$ at a current density of 3 350 $mA \cdot g^{-1}$ (2C). The research provides an effective approach for the preparation of high-performance sulfur cathodes based on tubular transition metal oxides with functionalizing conducting polymer, manifesting a promising pattern to achieve perfect stability, excellent reversibility, fast kinetics, high energy density and long cycle life for Li-S batteries.

Supporting information is available at http://www.wjhxxb.cn

References:

[1] Chen Y, Choi S H, Su D W, et al. *Nano Energy*, **2018**,**47**:331-339

[2] Yang Y, Zheng G Y, Cui Y. *Chem. Soc. Rev.*, **2013**,**42**:3018-3032

[3] Manthiram A, Fu Y Z, Chung S H, et al. *Chem. Rev.*, **2014**, **114**:11751-11787

[4] Cheng Z B, Pan H, Xiao Z B, et al. *J. Mater. Chem. A*, **2018**, **6**:7375-7381

[5] LI Yan-Bing(李严冰), DUAN Xiao-Bo(段晓波), HAN Ya-Miao(韩亚苗), et al. *Chinese J. Inorg. Chem.*(无机化学学报), **2015**,**31**(4):641-648

[6] Chen T, Ma L B, Cheng B R, et al. *Nano Energy*, **2017**,**38**: 239-248

[7] Ma L B, Zhang W J, Wang L, et al. *ACS Nano*, **2018**,**12**: 4868-4876

[8] ZHAO Bin(赵斌), LI Nian-Wu(李念武), LÜ Hong-Ling(吕洪岭), et al. *Chinese J. Inorg. Chem.*(无机化学学报), **2014**,**30**(4):733-740

[9] WANG Ying(王瑛), MI Kan(弭侃), XIONG Sheng-Lin(熊胜林). *Chinese J. Inorg. Chem.*(无机化学学报), **2017**,**33**(2): 243-248

[10]Wei Y J, Kong Z K, Pan Y K, et al. *J. Mater. Chem. A*, **2018**,**6**:5899-5909

[11]Wang M R, Zhang H Z, Zhou W, et al. *J. Mater. Chem. A*, **2016**,**4**:1653-1662

[12]Cha E, Patel M D, Park J, et al. *Nat. Nanotechnol.*, **2018**, **13**:337-344

[13]Xiao S, Liu S H, Zhang J Q, et al. *J. Power Sources*, **2015**, **293**:119-126

[14]Kim H, Lim H D, Kim J, et al. *J. Mater. Chem. A*, **2014**,**2**: 33-47

[15]Evers S, Nazar L F. *Acc. Chem. Res.*, **2013**,**46**:1135-1143

[16]Pu J, Shen Z H, Zheng J X, et al. *Nano Energy*, **2017**,**37**:7-14

[17]Xiao Z C, Kong D B, Song Q, et al. *Nano Energy*, **2018**,**46**: 365-371

[18]Yang W, Yang W, Song A L, et al. *Nanoscale*, **2018**,**10**:816-824

[19]Gueon D, Hwang J T, Yang S B, et al. *ACS Nano*, **2018**,**12**: 226-233

[20]Kang W M, Fan L L, Deng N P, et al. *Chem. Eng. J.*, **2018**, **333**:185-190

[21]Perez S B, Balbuena P B. *ChemSusChem*, **2018**,**11**:1970-1980

[22]Song J C, Noh H J, Lee J H, et al. *J. Power Sources*, **2016**, **332**:72-78

[23]Zhang M, Meng Q H, Ahmad A, et al. *J. Mater. Chem. A*, **2017**,**5**:17647-17652

[24]Yan J H, Li B Y, Liu X B. *Nano Energy*, **2015**,**18**:245-252

[25]Zhang S S, Tran D T, Zhang Z C. *J. Mater. Chem. A*, **2014**, **2**:18288-18292

[26]Hu H, Cheng H Y, Liu Z F, et al. *Nano Lett.*, **2015**,**15**:5116-5123

[27]Tsao C H, Hsu C H, Zhou J D, et al. *Electrochim. Acta*, **2018**,**276**:111-117

[28]Shen J D, Liu J, Liu Z B, et al. *Chem. Eur. J.*, **2017**,**24**:4573-4582

[29]Hong X J, Tang X Y, Wei Q, et al. *ACS Appl. Mater. Interfaces*, **2018**,**10**:9435-9443

[30]Yan M, Zhang Y, Li Y, et al. *J. Mater. Chem. A*, **2016**,**4**:9403-9412

[31]Fang M M, Chen Z M, Liu Y, et al. *J. Mater. Chem. A*, **2018**,**6**:1630-1638

[32]Hong Y J, Roh K C, Kang Y C. *Carbon*, **2018**,**126**:394-403

[33]Li W, Hicks-Garner J, Wang J, et al. *Chem. Mater.*, **2014**,**26**:3403-3410

[34]Liu X Y, Shan Z Q, Zhu K L, et al. *J. Power Sources*, **2015**, **274**:85-93

[35]Ma L, Wei S Y, Zhuang H L, et al. *J. Mater. Chem. A*, **2015**,**3**:19857-19866

[36]Paolella A, Laul D, Timoshevskii V, et al. *J. Phys. Chem. C*, **2018**,**122**:1014-1023

[37]Yuan Z, Peng H J, Hou T Z, et al. *Nano Lett.*, **2016**,**16**:519-527

[38]Lee J Y, Hwang T J, Lee Y H, et al. *Mater. Lett.*, **2015**,**158**:132-135

[39]Li Z, Zhang J T, Lou X W. *Angew. Chem. Int. Ed.*, **2015**,**54**:12886-12890

[40]Kong W B, Yan L J, Luo Y F, et al. *Adv. Funct. Mater.*, **2017**,**27**:1606663

[41]Zhang J, Shi Y, Ding Y, et al. *Nano Lett.*, **2016**,**16**:7276-7281

[42]Zefirov V V, Elmanovich I V, Levin E E, et al. *J. Mater. Sci.*, **2018**,**53**:9449-9462

[43]Luo J, Zhu H T, Fan H M, et al. *J. Phys. Chem. C*, **2008**, **112**:12594-12598

[44]Anilkumar K M, Jinisha B, Manoj M, et al. *Appl. Surf. Sci.*, **2018**,**442**:556-564

[45]Ji T, Tan L C, Hu X T, et al. *Phys. Chem. Chem. Phys.*, **2015**,**17**:4137-4145

[46]Reyes-Reyes M, Cruz-Cruz I, López-Sandoval R. *J. Phys. Chem. C*, **2010**,**114**:20220-20224

[47]Sakamoto S, Okumura M, Zhao Z, et al. *Chem. Phys. Lett.*, **2005**,**412**:395-398

[48]Chabu J M, Zeng K, Walle M D, et al. *Chemistry Select*, **2017**,**2**:11035-11039

[49]Ni L B, Zhao G J, Yang G, et al. *ACS Appl. Mater. Interfaces*, **2017**,**9**:34793-34803

[50]Rehman S, Tang T Y, Ali Z S, et al. *Small*, **2017**,**13**:1700087 (8 Pages)

[51]Su Y S, Fu Y Z, Cochell T, et al. *Nat. Commun.*, **2013**,**4**:2985-2992

[52]Zhao C C, Shen C, Xin F X, et al. *Mater. Lett.*, **2014**,**137**:52-55

[53]Fang R P, Zhao S Y, Hou P X, et al. *Adv. Mater.*, **2016**,**28**:3374-3382

[54]Ahn W, Kim K B, Jung K N, et al. *J. Power Sources*, **2012**, **202**:394-399